Mon. Not. R. Astron. Soc. **351,** 1247–1265 (2004) doi:10.1111/j.1365-2966.2004.07864.x

Structure and kinematics of edge-on galaxy discs – I. Observations of the stellar kinematics

M. Kregel,[1] P. C. van der Kruit[1]★ and K. C. Freeman[2]

[1]*Kapteyn Astronomical Institute, University of Groningen, PO Box 800, 9700AV Groningen, the Netherlands*
[2]*Research School for Astronomy & Astrophysics, Mount Stromlo Observatory, The Australian National University, Private Bag, Weston Creek, Canberra, ACT 2611, Australia*

Accepted 2004 March 19. Received 2004 March 19; in original form 2004 March 1

ABSTRACT

We present deep optical long-slit spectra of 17 edge-on spiral galaxies of intermediate to late morphological type, mostly parallel to their major axes and in a few cases parallel to the minor axes. The line-of-sight stellar kinematics are obtained from the stellar absorption lines using the improved cross-correlation technique. In general, the stellar kinematics are regular and can be traced well into the disc-dominated region. The mean stellar velocity curves are far from solid-body, indicating that the effect of dust extinction is not large. The line-of-sight stellar disc velocity dispersion correlates with the galaxy maximum rotational velocity, but detailed modelling is necessary to establish whether this represents a physical relation. In four spirals with a boxy- or peanut-shaped bulge we are able to detect asymmetric velocity distributions, having a common signature with projected radius in the mean line-of-sight velocity and the h_3 and h_4 curves. In two cases this kinematic asymmetry probably represents the 'figure-of-eight' pattern synonymous with a barred potential. We emphasize, however, that the signatures seen in the h_3 and h_4 curves may also be due to the disc seen in projection.

Key words: galaxies: fundamental parameters – galaxies: kinematics and dynamics – galaxies: spiral – galaxies: structure.

1 INTRODUCTION

The structure, kinematics and dynamics of discs in spiral galaxies have been and remain topics of much interest. Although much progress has been made in recent years (see e.g. Da Costa & Jerjen 2002), many questions remain, some of which are the following. Does the stellar disc thickness relate to the physical size of the galaxy? Is the flattening of the disc linked to other global galaxy properties? At what radius do stellar discs truncate and why? Is there indeed a trend between the amount of random stellar motions and the rotational velocity of a galaxy? If so, what is the physical cause of this relation? Is the matter in the disc sufficient to explain the rotation curve in the inner parts of spiral galaxies? Finally, how do the answers to the above questions change for discs of lower surface brightness? In this series of papers,[1] we aim to provide new constraints on the dynamics of spiral galaxy discs through an observational synthesis of the global stellar disc structure and kinematics. The importance of the vertical disc structure for estimating disc masses automatically leads us toward edge-on systems. The wish to study 'pure' discs further narrows the focus toward undisturbed spirals of intermediate to late Hubble type. By combining photometry, absorption-line spectroscopy and H I synthesis observations for a substantial sample of such systems, the properties of galaxy discs can be probed over a large range in maximum rotational velocity and surface brightness. For such a sample, optical and near-infrared photometry has been analysed by de Grijs (1997, 1998). This sample has been adopted as a starting point for the present study and has been re-analysed by Kregel, van der Kruit & de Grijs (2002). That paper is a prologue to this series and will be referred to as KKG.

This first paper in the series is concerned with the kinematics of the evolved stellar population of galaxy discs. The stellar velocity distribution contains valuable information regarding the disc mass distribution (van der Kruit & Freeman 1986; Bottema 1993), the mechanisms responsible for disc heating (Gerssen, Kuijken & Merrifield 1997, 2000), and the stability properties of discs which are widely believed to regulate star formation (Wang & Silk 1994; Martin & Kennicutt 2001). A full understanding of these fundamental but elusive disc properties requires a synthesis of the kinematics and the three-dimensional structure of stellar discs. In KKG, the stellar disc flattening was used to re-estimate the disc contribution to the rotation curve, based on the empirical relation between stellar velocity dispersion and maximum rotational velocity in unbarred high surface brightness (HSB) spirals (Bottema 1993). Unfortunately, this σ–$v_{\rm max}$ relation is still ill-constrained because

★E-mail: vdkruit@astro.rug.nl

[1] The series contains adapted versions of most chapters in the PhD thesis of MK (Kregel 2003).

of the small number of spirals for which the stellar disc velocity dispersions are known (Bottema 1993; Gerssen, Kuijken & Merrifield 1997, 2000; Pignatelli et al. 2001), causing a significant uncertainty in the derived result. In addition, the observed correlation between the disc flattening and the global ratio of dark to luminous matter [Zasov et al. 2002; Kregel 2003; Paper V in this series (Kregel, van der Kruit & Freeman, in preparation)] suggests a more complicated picture, in which the face-on central surface brightness performs the role of a third parameter in the σ–$v_{\rm max}$ relation. Enlarging the sample of spiral galaxies with measured stellar disc kinematics is needed to improve the statistics on the σ–$v_{\rm max}$ relation and to study the relative importance of the disc mass among spiral galaxies.

In this paper we present deep spectroscopic observations of 17 edge-on spirals of intermediate to late morphological type. For most of these spirals the slit was placed parallel to and away from the major axis during the observations to avoid the bulk of the dust and to study the radial variation of the stellar disc kinematics. In three spirals the slit was placed parallel to the minor axis at a projected radius of one disc scalelength to monitor the effect of dust extinction on the disc kinematics. We extract the line-of-sight (l.o.s.) stellar kinematics from the stellar absorption lines in the 4800–5800 Å region using the cross-correlation technique. This technique is well suited for handling the spectra of galaxy discs (Bottema 1988; Bender 1990; Statler 1995), which are currently still in the regime of low signal-to-noise ratio and poor spectral sampling. The stellar kinematics derived here will be used in conjunction with the global disc structure (KKG) and the circular velocity curves from H I and optical emission-line spectroscopy [Papers II (Kregel, van der Kruit & de Blok 2004) and III (Kregel & van der Kruit 2004)] to study the intrinsic stellar disc velocity dispersion [Paper IV (Kregel & van der Kruit, in preparation)]. We will present a general discussion in Paper V.

Focusing on edge-on spirals has several advantages. As far as photometry is considered they allow the study of the full 3D distribution of the stellar light (van der Kruit & Searle 1981a,b, 1982). For our kinematic studies edge-on galaxies are particularly useful for the following reasons. First, edge-on spirals have a higher surface brightness by virtue of their orientation, allowing the observation of a substantial sample within a short amount of observing time. This effect also facilitates the study of the stellar kinematics in discs with a low *face-on* surface brightness. Secondly, the edge-on orientation has the advantage that young stellar populations can be largely avoided by placing the slit away from the galactic plane, reducing possible systematics related to template mismatch. Finally, the galaxy orientation also means that effectively the entire galaxy plane is sampled by a single slit, such that local deviations from axisymmetry in the stellar structure and kinematics are largely averaged out. The obvious disadvantage of edge-on spirals is that the l.o.s. projection has to be taken into account when interpreting the observed stellar kinematics. However, it is possible to disentangle the observed kinematics and the l.o.s. effects using a realistic dynamical disc model and circular velocity curve (Bottema, van der Kruit & Freeman 1987; Bottema, van der Kruit & Valentijn 1991).

The galaxy properties are summarized in Section 2. In Section 3, we present the observations, outline the data reduction and describe the cross-correlation technique. This includes a comparison with three alternative methods for obtaining the stellar kinematics and a brief discussion on the effects of template mismatch. The derived l.o.s. stellar kinematics are presented together with notes on each individual galaxy in Section 4. The observations are discussed in Section 5, focusing on global trends and the presence of conspicuous asymmetries in the l.o.s. velocity distributions. Finally, Section 6 summarizes the main results. Throughout this series distances are calculated using the Virgo-centric velocities from the Lyon/Meudon Extragalactic Data base (LEDA, recently incorporated in HyperLeda; see table 1 in KKG) and a Hubble constant $H_0 = 75$ km s^{-1} Mpc^{-1}.

2 THE SAMPLE

The sample consists of a subset of the sample studied by KKG plus the three large, well-studied spirals NGC 891, 5170 and 5529. We added these three spirals to allow us to study the stellar kinematics in finer detail, especially regarding its variation with projected radius and height above the galactic plane. The selection of the galaxies from KKG for spectroscopic observations was mainly influenced by the allocation of observing time. Important properties of the observed spirals are listed in Table 1. The sample is well suited for a study of the stellar disc kinematics among spiral galaxies: it is dominated by intermediate- to late-type spirals, such that bulge contamination is small, while both the maximum rotational velocity and the disc flattening cover a wide range. We note that, although there are no barred galaxies in the sample according to the LEDA classification, there are several candidates that display a boxy or peanut-shaped bulge (fig. A1 in KKG, marked by an asterisk in Table 1). Of these, ESO 437-G62 has an extremely low H I content for its rotation velocity (see table 1 in KKG, Kregel 2003) and would fit better in the S0 class.

3 OBSERVATIONS AND DATA REDUCTION

3.1 The observations

The long-slit spectra were obtained during five observing runs at the 2.3-m telescope (SSO 2.3 m) at Siding Spring (Australia), two runs at the 4.2-m William Herschel Telescope (WHT) on La Palma (Spain), and service mode observations at the 8.2-m Unit Telescope 2 (Kueyen) of the Very Large Telescope (VLT) on Paranal (Chile). The observations were carried out in dark time to minimize the sky background. At Siding Spring, the Double Beam Spectrograph (DBS) was used with a dichroic to observe simultaneously in two wavelength regions. The blue arm of the DBS was tuned to record the 4800–5800 Å region, which contains the characteristic Mg I b triplet, numerous strong Fe I absorption lines and the Hβ and [O III] 4959,5007-Å emission lines. The red arm registered the Hα, [N II] 6548,6583-Å and [S II] 6716,6731-Å emission lines. The same approach was taken with the ISIS spectrograph at the WHT. At Paranal, FORS2 covered the blue region using the holographic 1400V grism. This grism has an efficiency of $\sim$90 per cent in the V band. The spectral resolution of the obtained spectra is in the range 0.8–1.2 Å FWHM in the blue (50–75 km s^{-1} FWHM). The exact wavelength setup and a log of the observations are presented in Table 2, while details of the instruments are summarized in Table 3.

The observing runs at the SSO 2.3-m and the WHT proceeded as follows. During the afternoon setup, care was taken to align the dispersion axis with the image rows. At evening twilight a number of spectra were taken of an essentially blank piece of sky, followed by spectra of at least two bright stars close to MK type K0 III. These stars dominate the integrated light of old stellar populations and are therefore commonly used as templates in the cross-correlation analysis (see Section 3.5). For these stars the telescope was de-focused to obtain a uniform illumination on the slit. The exposure times of the template spectra were maximized by trailing the star along part of the slit during the exposure; the final template spectra are essentially noise-free. In photometric conditions a spectrophotometric

Table 1. Properties of the sample galaxies.

Galaxy		Type	$v_{\rm vir}$ (km s^{-1})	M_I^0 (mag)	$v_{\rm max}$ (km s^{-1})	$h_{{\rm R},I}$ (kpc)	$(h_{\rm R}/h_z)_I$
(1)		(2)	(3)	(4)	(5)	(6)	(7)
ESO 142-G24	IC 4872	Scd	2496	−19.54	99	4.3	7.0
ESO 157-G18	IC 2058	Scd	1103	−18.55	89	2.6	7.6
ESO 201-G22		Sc	3819	−20.43	155	6.0	8.4
ESO 240-G11*		Sc	2656	−21.65	260	8.4	14.0
ESO 269-G15	NGC 4835A	Sc	3191	−21.16	155	5.9	6.9
ESO 288-G25		Sbc	2333	−20.84	164	2.8	7.4
ESO 416-G25*		Sb	4812	−21.53	204	7.1	6.0
ESO 435-G14		Sc	2482	−20.11	124	2.8	5.3
ESO 435-G25*	IC 2531	Sc	2290	−21.46	231	14.4	19.4
ESO 437-G62*	NGC 3390	Sb	2860	−22.30	209	6.6	5.4
ESO 446-G18*		Sb	4661	−21.34	189	7.8	12.9
ESO 487-G02*	NGC 1886	Sbc	1558	−20.17	162	2.5	6.4
ESO 509-G19		Sbc	10574	−23.51	392	17.0	9.9
ESO 564-G27		Sc	2020	−19.93	152	5.0	10.9
NGC 891*		Sb	691	−21.36	212	4.8	13.0
NGC 5170		Sc	1431	−21.75	238	6.5	7.8
NGC 5529*		Sc	3070	−22.32	274	5.9	10.2

Columns. (1) Name: an asterisk marks a galaxy with a boxy- or peanut-shaped bulge. (2) Hubble type (LEDA). (3) Heliocentric velocity corrected for Virgo-centric flow (LEDA). (4) I-band absolute magnitude, calculated using the apparent magnitude (de Grijs 1998) and $H_0 = 75$ km s^{-1} Mpc^{-1}, and corrected for Galactic extinction. For NGC 891 and 5529 an apparent magnitude was provided by Xilouris (private communication). (5) Maximum rotational velocity (LEDA), obtained from global H I profiles and corrected for turbulent motions. For ESO 288-G25 $v_{\rm max}$ is unavailable and was estimated using a least-squares fit to the Tully–Fisher relation defined by columns (4) and (5). (6) I-band scalelength in kpc (KKG). (7) Disc flattening in the I band (KKG). For NGC 891 and 5529 the scale parameters were taken from Xilouris et al. (1999); for NGC 5170 they are presented in Appendix A.

standard was taken. Single exposures of the galaxy were limited to 1800–2000 s to avoid excessive cosmic ray contamination, and were bracketed by exposures of an arc lamp for accurate wavelength calibration. The total exposure time on the galaxy was determined by requiring that a reasonable amount of additional spatial binning of the final spectrum is able to yield a signal-to-noise ratio (SNR) in the range 10–20 per spectral pixel. Finally, during twilight or daytime, spectra of a tungsten lamp were taken for flat-fielding, together with a number of bias and dark frames. To minimize read-out noise we used on-chip binning at the WHT, taking a 5×2 binning scheme (spatial $\times$ spectral) in 2000 July (NGC 5529) and a 5×1 scheme in 2000 November (NGC 891). In the spectrum taken parallel to the major axis of NGC 891 the galaxy light dominates along the entire length of the slit. In this case a 600-s spectrum of a neighbouring piece of sky was taken after each galaxy exposure to serve for the sky background subtraction.

The VLT observations were carried out in service mode. Ironically, observing regulations did not allow us to de-focus the telescope. To still obtain a uniform slit illumination for the stellar spectra, the observations were performed during relatively poor seeing conditions. The lower spatial resolution is not a problem because additional spatial binning is required to provide a sufficient SNR. To reach an adequate spectral resolution the narrow 0.51-arcsec slit was used, which has the additional advantage that the spectra sample a small vertical range. Standard FORS2 calibrations included arc lamp exposures, bias frames and screen flats, and were augmented with twilight flats and dark frames.

In most cases the slit was positioned parallel to the major axis and away from the dust lane, when present. In three galaxies the slit was positioned parallel to the minor axis at a projected radius of one disc scalelength to avoid the bulge-dominated region. At the SSO 2.3-m and the WHT a star was included in the slit for accurate positioning. At the VLT the acquisition images allow accurate ($\sim$0.2 arcsec) positioning. The exact slit positions are listed in Table 4.

3.2 The data reduction

The data reduction was carried out using 'standard' IRAF procedures in the LONGSLIT and RV packages. For the DBS and ISIS spectra these were carried out separately for the data from the blue and the red arm. First, the bias pedestal was removed using the overscan region. The dark current proved to be negligible. To create a flat-field, first the median of the tungsten lamp exposures was formed. The large-scale wavelength response from the lamp was removed by fitting and subsequently dividing a low-order polynomial. The lamp-corrected median flat was divided into the science and calibration frames, removing the pixel-to-pixel gain variations. The twilight frames were combined and inspected and used to correct for vignetting when significant. Cosmic rays were removed using the COSMIC algorithm in MIDAS.

Dispersion solutions were determined for each arc frame by fitting a fourth-order polynomial to about 20 bright emission lines. For the DBS the root-mean-square (r.m.s.) wavelength residuals were typically 0.04 Å in the blue and 0.02 Å in the red arm, for ISIS these residuals were about 0.02 and 0.01 Å and for FORS2 they were only $\sim$0.005 Å. These two-dimensional dispersion solutions were then used to calculate the coordinate transformation needed to rectify the data in the dispersion direction. The spectrophotometric standard was traced in the wavelength direction to map the distortion in the spatial direction (the 'S-shape' distortion). The two-dimensional dispersion and the S-shape solutions were used to map the CCD pixel coordinates to position versus logarithmic wavelength coordinates (so that a pixel shift corresponds to a linear velocity shift). The

Table 2. Observing log.

Galaxy	Date	Telescope	Orient.*	Exposed	λ-range†	Slit width	Seeing (FWHM)	Resolution† (FWHM)	Scale (log λ)†
				s	(Å)	(arcsec)	(arcsec)	(km s^{-1})	(km s^{-1})
ESO 142-G24	1999 May 14,15	SSO 2.3 m	∥	3 × 2000	4785–5752, 6005–6958	2.0	2.0–5.0	82, 61	31.5866, 25.2771
ESO 157-G18	2000 Oct. 28,29	Kueyen	∥	2 × 1800	4720–5760	0.51	0.7	66	29.1633
ESO 201-G22	2000 Jan. 10,11	SSO 2.3 m	∥	14 × 2000	4785–5742, 6020–6972	2.0	2.0–3.0	70, 61	31.2871, 25.1940
ESO 240-G11	1999 Aug. 13	SSO 2.3 m	∥A	4 × 2000	4785–5752, 6005–6958	2.0	2.5–3.5	101, 73	31.5866, 25.2771
	2000 Oct. 28	Kueyen	∥B	3 × 1800	4720–5760	0.51	1.0	68	29.1633
ESO 263-G15‡	2001 Feb. 25,26	SSO 2.3 m	∥	8 × 2000	4785–5752, 6005–6958	2.0	2.9–3.9	92, 61	31.5866, 25.2771
ESO 269-G15	2001 Jan. 1, 2001 Feb. 18	Kueyen	∥	3 × 1800	4720–5760	0.51	0.9	63	29.1633
ESO 288-G25	1999 Aug. 11	SSO 2.3 m	∥	3 × 2000	4785–5752, 6005–6958	1.8	2.8	74, 56	31.5866, 25.2771
ESO 416-G25	2000 Oct. 28	Kueyen	∥	2 × 1800	4720–5760	0.51	0.7	68	29.1633
ESO 435-G14	2000 Dec. 31	Kueyen	∥	4 × 1800	4720–5760	0.51	0.7	68	29.1633
ESO 435-G25	2001 Jan. 1	Kueyen	∥	1 × 1800	4720–5760	0.51	0.8	64	29.1633
ESO 435-G50‡	2001 Feb. 24	SSO 2.3 m	∥	12 × 2000	4785–5752, 6005–6958	2.0	2.9–3.9	92, 61	31.5866, 25.2771
ESO 437-G62	2001 Jan. 1	Kueyen	∥	2 × 1800	4720–5760	0.51	1.0	64	29.1633
ESO 446-G18	2001 Feb. 18	Kueyen	∥	2 × 1800	4720–5760	0.51	0.8	63	29.1633
ESO 487-G02	2000 Jan. 12	SSO 2.3 m	⊥	5 × 2000	4785–5742, 6020–6972	2.0	2.0–3.0	70, 61	31.2871, 25.1940
FESO 509-G19	2001 Feb. 18	Kueyen	∥	1 × 1800	4720–5760	0.51	0.7	63	29.1633
ESO 564-G27	2000 Jan. 11,12	SSO 2.3 m	∥	11 × 2000	4785–5742, 6020–6972	2.0	3.0–4.0	70, 61	31.2871, 25.1940
NGC 891	2000 Nov. 26–27	WHT	∥	9 × 1800	4752–5664, 6400–6800	1.3	2.0–2.4	52, 36	25.7122, 17.7661
	2000 Nov. 26–27	WHT	⊥	13 × 1800	4752–5664, 6400–6800	1.3	2.0–2.4	52, 36	25.7122, 17.7661
NGC 5170	1999 Apr. 10,11	SSO 2.3 m	⊥A	10 × 2000	4785–5750, 6020–6975	2.5	2.0–2.5	76, 66	31.5260, 25.2678
	1999 Apr. 10,11	SSO 2.3 m	⊥B	19 × 2000	4785–5750, 6020–6975	2.5	2.0–2.5	76, 66	31.5260, 25.2678
NGC 5529	2000 Jul. 1,2	WHT	∥	10 × 1800	4767–5645, 6400–6800	1.2	0.9	51, 41	12.9170, 17.7661

*Orientation with respect to the galaxy major axis. Exact positions and position angles are listed in Table 4. †Values are for the blue and the red arm, respectively. ‡The spectra of these two galaxies were of insufficient quality to analyse the absorption lines. They are listed because they will be used to study the emission-line kinematics (Paper III).

Table 3. Instruments and setup.

Parameter	Telescope				
	SSO 2.3 m		WHT		VLT–Kueyen
Spectrograph	DBS		ISIS		FORS2
Slit length (arcmin)	6.7		3.7		6.8
Dichroic	D3 (6300 Å)		6100		–
	Blue arm	Red arm	Blue arm	Red arm	
Grating*	1200B	1200R	R1200B	R1200R	GRIS 1400V+18
Detector	SITe (CCD7)	SITe (CCD9)	EEV12	TEK4	TEK
Format	1752 × 532	1752 × 532	4096 × 2048	1024 × 1024	2048 × 2046
Pixel size	15 μm	15 μm	13.5 μm	24 μm	24 μm
Gain (e^- ADU^{-1})	1.0	1.0	1.01	1.6	1.91
Readout noise (e^-)	5.5	6.0	3.9	4.1	5.41
Scale (arcsec $pixel^{-1}$)	0.90	0.91	0.19†	0.33	0.20
Dispersion (Å $pixel^{-1}$)	0.55	0.55	0.23†	0.41	0.50
Arc lamp	Ne–Ar	Ne–Ar	Cu–Ar	Cu–Ne	Hg–Cd+2

*All observations were carried out in first order. †See text for binning schemes adopted with ISIS blue.

logarithmic bin size (Table 2) was chosen to preserve the number of spectral pixels.

All galaxy spectra taken within the same night were then added, and heliocentric velocity corrections were calculated. For galaxy positions observed during multiple nights the spectra were re-aligned in velocity when the difference between the heliocentric corrections was larger than the rms wavelength error, and spatially using either a star or the peak of the galaxy continuum. The sky emission in the combined galaxy spectra was estimated by fitting a zeroth- or first-order polynomial to the outer source-free parts of the slit, and subtracted. A similar procedure was used for the template stars. For the major axis position of NGC 891 the sky was determined by combining the separate sky spectra, scaling the result to the total galaxy exposure time, and averaging along the slit. This sky spectrum was sufficiently flat along the slit that it can be taken as a good substitute of the sky in the actual spectrum of NGC 891. The averaging produced an essentially noise-free sky spectrum, so that no further noise was introduced. Finally, the radial velocities of the template stars were determined from the average of the wavelength shifts of 12 strong absorption lines. The errors of the template velocities are 1–2 km s^{-1}. The stellar absorption lines in the 4800–5800 Å region will be the subject of this paper. The emission lines in both the 4800–5800 and the 6000–7000 Å regions will be studied separately in Paper III.

3.3 The cross-correlation technique

A spectrum taken at a position in a galaxy is the sum of the spectra of its constituent stars, each stellar spectrum being Doppler-shifted according to its l.o.s. velocity and weighted according to the details of the radiative transfer (extinction by dust). Under the assumption that the galaxy spectrum can be described by that of a single star, the galaxy spectrum is simply the convolution of the spectrum of a template star with the l.o.s. velocity distribution (LOSVD). Simkin (1974) first used the cross-correlation function (XCF) between the galaxy and template spectra to measure radial velocities from the position of its peak, and Tonry & Davis (1979) first estimated the velocity dispersion from a comparison of the widths of this XCF and the autocorrelation function (AXF) of the template spectrum. This cross-correlation approach has been improved to retrieve the LOSVD either by fitting the peak of the XCF with a broadened ACF (Bottema 1988; Bender 1990; Statler 1995) or by straight deconvolution of the peak using the CLEAN algorithm (Franx & Illingworth 1988).

Unlike elliptical galaxies and bulges, galaxy discs are dynamically cool and typically have surface brightnesses far below that of the night sky. With current instrumental capabilities, spectra of galaxy discs are characterized by SNRs of about 10–20 per spectral pixel. At these low SNRs it is not possible to minimize the error due to template mismatch by constructing an ideal template from a mixture of stellar types (Rix & White 1992). In this case the cross-correlation (XC) method is particularly useful (van der Kruit & Freeman 1986; Bottema 1988). The use of the XCF peak partly eliminates the coupling between the stellar kinematics and the spectral synthesis, making the XC method less sensitive to template mismatch than methods that directly rely on the galaxy spectrum (Bender 1990; Statler 1995). The least-squares fit also provides a reliable estimate of the errors and the goodness-of-fit, largely independent of template mismatch (Statler 1995; but see de Bruyne et al. 2003).

Before being able to calculate the XCF and ACF from the observed spectra and to perform the actual least-squares fits, the spectra need further processing to remove residual continuum variation. After binning, an estimate of the stellar continuum was obtained by fitting a low-order polynomial to each binned spectrum. This fit was subsequently divided into the spectrum, after which the mean was subtracted. To avoid aliasing and ringing during Fourier transformation, the outer 10 per cent of the spectra were end-masked using a cosine-bell curve. Remaining large-scale variations were then removed in the Fourier domain by padding the spectra with zeros up to wavenumber $k_{\rm taper}$ and using a cosine-bell taper up to wavenumber $2k_{\rm taper}$ (Brault & White 1971). Based on tests on artificially broadened template stars a value $k_{\rm taper} = 10$ was adopted for all our spectra. In the galaxy spectra regions containing emission lines or residuals from strong sky lines were put to zero. As an example and in order to illustrate the quality of our VLT–Kueyen spectra, a fully processed spectrum of ESO 435-G25 (IC 2531) is shown in Fig. 1. Finally, the noise in the prepared spectrum was estimated by quadratically adding the Poisson noise according to the photon counts from galaxy and sky to the read-out noise (taking into account the number of spectra that were combined). This noise spectrum was then processed in the same way as the galaxy spectrum.

Table 4. Positioning and cross-correlation parameters.

Galaxy	Orient.	Dynamical centre		Slit centre		d(slit–centre)*	Slit PA†	Template	Spectral type	SNR	LOSVD‡
		RA(J2000) ($^{h}\,^{m}\,^{s}$)	Dec.(J2000) ($^{d}\,^{m}\,^{s}$)	RA(J2000) ($^{h}\,^{m}\,^{s}$)	Dec.(J2000) ($^{d}\,^{m}\,^{s}$)	(arcsec)	(deg)				
ESO 142-G24	‖	19 35 42.24	−57 31 07.3	19 35 42.26	−57 31 07.7	+0.4 ± 2	5	HD 132667	G5 III	12	G
ESO 157-G18	‖	04 17 54.43	−55 55 55.2	04 17 54.01	−55 55 54.0	−3.7 ± 1	18.6	HD 13742	K0 III	15	G
ESO 201-G22	‖	04 08 59.90	−48 43 37.1	04 08 59.90	−48 43 36.7	+0.4 ± 1	60	HD 47371	K0 III	11	G
ESO 240-G11	‖A	23 37 49.41	−47 43 38.8	23 37 49.41	−47 43 38.8	0.0 ± 1	128	HD 176047	K0 III	7	G
	‖B			23 37 49.57	−47 43 37.0	+2.4	128.1	HD 13742	K0 III	$R < 20$ arcsec: 40 $R > 20$ arcsec: 20	GH
ESO 263-G15	‖	10 12 19.78	−47 17 40.6	10 12 19.72	−47 17 42.3	+1.8	288.9	–	–	–	–
ESO 269-G15	‖	12 57 13.17	−46 22 41.4	12 57 13.30	−46 22 41.4	+1.3 ± 1	358.8	HD 104807	K0 III	15	G
ESO 288-G25	‖	21 59 17.87	−43 52 01.3	21 59 17.89	−43 52 01.6	−0.4 ± 1	233.5	HD 176047	K0 III	12	G
ESO 416-G25	‖	02 48 40.70	−31 32 10.3	02 48 40.89	−31 32 11.5	+2.7	24.8	HD 13742	K0 III	15	GH
ESO 435-G14	‖	09 57 48.42	−28 30 23.7	09 57 48.46	−28 30 24.4	−0.9 ± 1	231.9	HD 88601	K0 III	20	G
ESO 435-G25	‖	09 59 55.37	−29 37 02.4	09 59 55.46	−29 37 06.7	−4.5 ± 1	254.8	HD 88601	K0 III	$R < 30$ arcsec: 15 $R > 30$ arcsec: 10	GH
ESO 435-G50	‖	10 10 50.11	−30 25 25.6	10 10 50.11	−30 25 25.6	0.0	70.1	–	–	–	–
ESO 437-G62	‖	10 48 04.37	−31 32 00.1	10 48 04.22	−31 32 00.2	+2.0 ± 1	178.8	HD 88601	K0 III	$R < 30$ arcsec: 30 $R > 30$ arcsec: 20	GH
ESO 446-G18	‖	14 08 38.30	−29 34 18.2	14 08 38.28	−29 34 18.2	+0.2 ± 1	186.3	HD 88601	K0 III	$R < 20$ arcsec: 12 $R > 20$ arcsec: 20	GH
ESO 487-G02	⊥	05 21 48.10	−23 48 35.3	05 21 49.36	−23 48 26.0	+19.2	333	HD 47371	K0 III	7	G
ESO 509-G19	‖	13 27 56.39	−25 51 22.5	13 27 56.41	−25 51 22.8	+0.4 ± 2	229.4	HD 88601	K0 III	5	G
ESO 564-G27	‖	09 11 54.72	−20 07 01.7	09 11 54.76	−20 07 01.8	+0.6 ± 2	347	HD 47371	K0 III	11	G
NGC 891	‖	02 22 33.28	+42 20 56.9	02 22 32.50	+42 20 59.7	−108 ± 1.5	202.8	HD 76629	G8 III	20	GH
	⊥			02 22 37.14	+42 22 36.1	+9.1	112.8	HD 76629	G8 III	10	G
NGC 5170	⊥A	13 29 48.75	−17 57 59.5	13 29 44.59	−17 57 15.9	+78	216	HD 23959	K2 III	8	G
	⊥B			13 29 41.00	−17 56 37.0	+142	216	HD 23959	K2 III	10	G
NGC 5529	‖	14 15 34.12	+36 13 37.5	14 15 34.10	+36 13 37.1	+0.5 ± 1.5	115.0	HD 165683	K0 III	15	GH

*Shortest angular distance between the adopted dynamical centre and the slit. A positive (negative) sign indicates that the slit is positioned towards the far (near) side of the galaxy. In cases where the slit was positioned perpendicular to the major axis, a positive (negative) sign indicates that the slit is positioned at the receding (approaching) side. The errors denote the adopted uncertainty in the dynamical centre (used in Paper IV). †Position angle (N → E) referring to the part of the slit at the receding side of the galaxy (‖) or simply to the slit (⊥, 180° ambiguity). ‡G – Gaussian (equation (4), GH – truncated Gauss–Hermite series (equation 5).

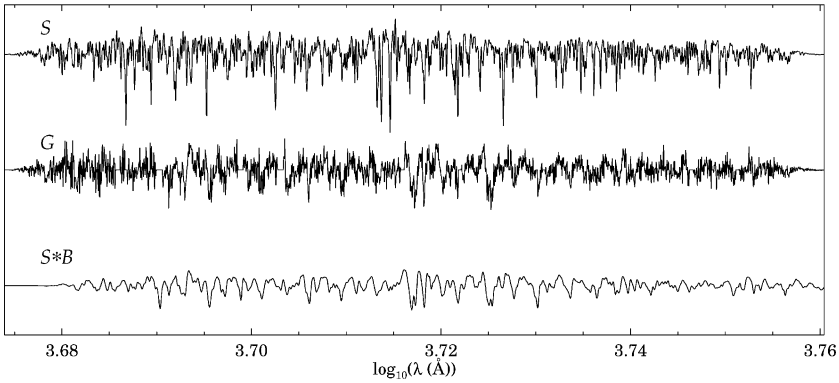

Figure 1. Example of fully processed spectra, taken with the VLT–Kueyen, showing the template HD 88601 (S) and a single position in ESO 435-G25 (G, corresponding to the bin centred at +11 arcsec, cf. Figs 2 and 5). The third spectrum ($S * B$) is that of the template HD 88601 but shifted and broadened according to the parametrized LOSVD (B) obtained from the XC analysis.

The cross-correlation and least-squares minimization were performed using the improved XC method (Statler 1995). Statler's IDL algorithm uses standard Fourier techniques to calculate cross-correlation functions, and the multi-dimensional simplex algorithm (Nelder & Mead 1965) to find the minimum χ^2. The XCF errors are estimated from the noise spectrum and used to calculate the covariance matrix of the least-squares fit (Statler 1995). For the actual fitting the region bounded by the first local minima on either side of the XCF peak is taken. For the LOSVD either a simple Gaussian,

$$B(v) = \frac{\gamma}{\sqrt{2\pi}\sigma_{\rm los}} \exp\left[-(v - v_{\rm los})^2 \big/ 2\sigma_{\rm los}^2\right], \quad (1)$$

or a truncated Gauss–Hermite series (van der Marel & Franx 1993),

$$B(v) = \frac{\gamma}{\sqrt{2\pi}\sigma_{\rm los}} \exp\left[-(v - v_{\rm los})^2 \big/ 2\sigma_{\rm los}^2\right] \times \{1 + h_3 H_3[(v - v_{\rm los})/\sigma_{\rm los}] + h_4 H_4[(v - v_{\rm los})/\sigma_{\rm los}]\}, \quad (2)$$

is used, where γ is the 'line strength', $v_{\rm los}$ is the mean l.o.s. velocity, $\sigma_{\rm los}$ is the l.o.s. velocity dispersion and H_3 and H_4 are the Hermite polynomials of the third and fourth degree. The h_3 parameter measures the skewness (a positive h_3 indicates a tail towards larger velocities) and the h_4 parameter measures the kurtosis (for positive h_4 the LOSVD has narrower wings than a Gaussian).

As an example, we consider the XCFs obtained from the FORS2 data of ESO 435-G25 and the K0 giant HD 88601 (Fig. 1). For the spatial binning a SNR of 15 was used up to 30 arcsec from the galaxy centre and, to reach the largest possible radii, a SNR of 10 further out (Table 4). Fig. 2 shows the XCFs and the fits obtained with the XC method using the truncated Gauss–Hermite series for the LOSVD. The corresponding results for the LOSVD parameters are shown in Fig. 5 (later) and will be discussed together with the results for the entire sample in Section 4. By viewing the XCFs it is already apparent that the mean velocity increases and that the velocity dispersion decreases with radius. In addition, at radii up to 30–40 arcsec the XCFs are clearly asymmetric, showing a tail towards velocities away from the systemic velocity.

3.4 A comparison with alternative methods

To assess the reliability of the XC method, we compared its results with those obtained with several other attested methods. Fig. 3 shows the l.o.s. stellar kinematics of NGC 5170 (along position A, see Table 2 and Fig. 5, later) according to four entirely different methods, under the assumption of a Gaussian LOSVD and using HD 023959 (a K2 giant) as a template. The applied methods are the XC method, unresolved Gaussian decomposition (UGD: Kuijken & Merrifield 1993), the cross-correlation clean technique (CCC: Franx & Illingworth 1988; Bottema 1999) and direct pixel fitting (PF: van der Marel 1994). For more details on the implementation of these techniques see Kregel (2003).

UGD is a non-parametric method which models the LOSVD as the sum of a set of unresolved Gaussians, uniformly spaced in velocity. The UGD software was run using Gaussians separated by 2 pixel and with a dispersion of 4/3 pixel (the spectral resolution corresponds to 2.5 pixel). To be able to include the UGD result in the comparison, Gaussians were fitted to the non-parametric UGD estimates of the LOSVDs. The CCC method was applied to the cross-correlation peaks, cleaning down to a level well below the noise. The clean components were restored using a Gaussian 'clean beam' with a dispersion of 2.5 pixel, and added to the residuals to yield the CCC estimate of the (resolution broadened) LOSVD. Following standard practice, the restored peak was then fitted with a Gaussian, taking the rms value of the XCF away from the XCF peak for the errors on the restored peak. Finally, the fitted dispersion was corrected for the velocity resolution of the 'clean beam'. The PF method models the galaxy spectrum as the sum of a broadened template spectrum and a number of continuum terms using the Legendre polynomials. The PF method was applied using six continuum terms and excluding the outermost short-wavelength end for which no template information is available.

The mean l.o.s. velocities obtained with all four methods are in excellent agreement (Fig. 3); no systematic offsets are detected. In addition, the velocity errors also agree well, although the errors obtained with the CCC method are slightly smaller than those of the other three methods. The velocity dispersions and their errors are also in good agreement, except for the values of the CCC method at −4 and −6 arcsec. There the CCC method seems to have overestimated the velocity dispersion. We conclude that the XC method is reliable and that the additional data processing required for the XC method introduces no (measurable) systematics.

3.5 The template mismatch

The issue of mismatch needs to be considered as a final source of systematic error. To assess this error the XC method was tested on synthetic galaxy spectra constructed using five stellar spectra

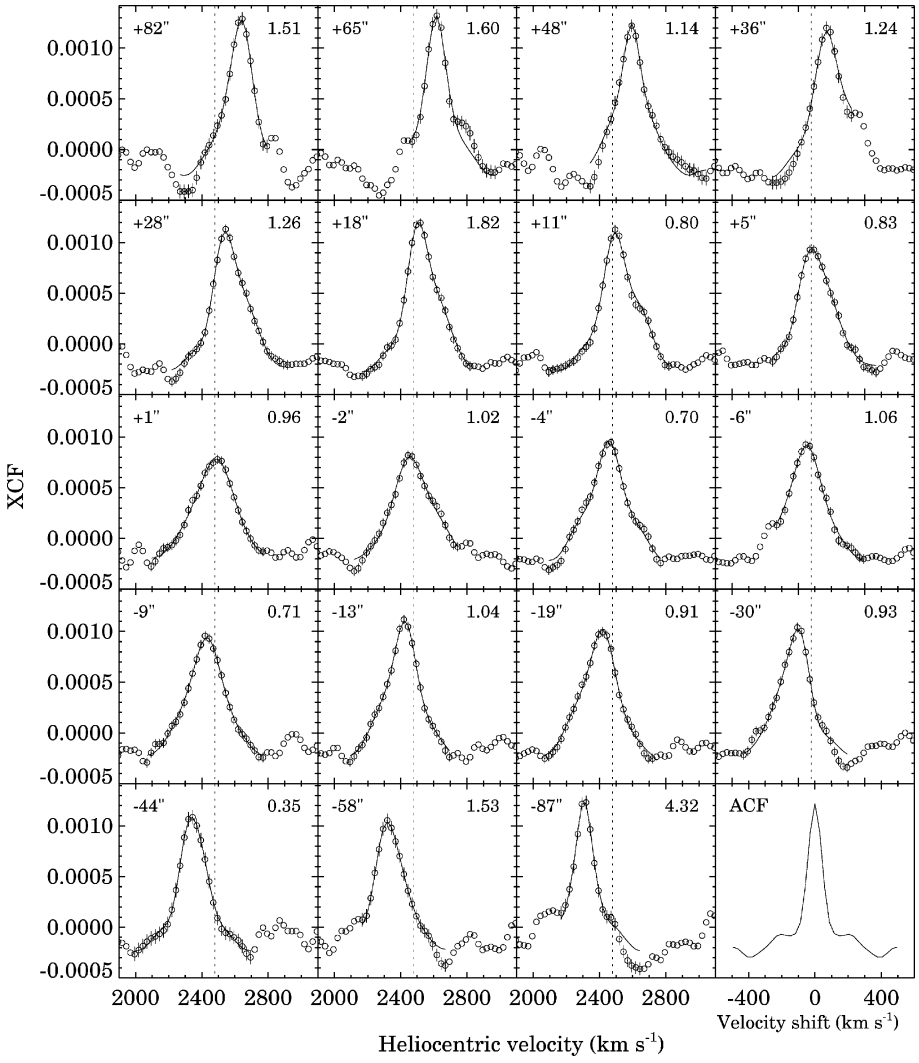

Figure 2. Cross-correlation functions for ESO 435-G25 (circles) and least-squares fits (solid lines), shown for every second bin along the slit (cf. Fig. 5). The fit and the XCF errors are plotted only in the fitted region. The intensity-weighted position of each bin is shown in the upper left of each panel. The upper right corner shows the reduced χ^2 of each fit. The H I systemic velocity (see Paper II) is indicated by the dotted line. The bottom right panel shows the template ACF.

obtained during the 2000 November WHT run: HD 076629 (G8 III), HD 166207 (K0 III), HD 075523 (K0 III), HD 001527 (K1 III) and HD 166229 (K2 III). The logarithmic wavelength scale of these spectra is 25.7 km s^{-1} pixel^{-1}. The stellar spectra were convolved with Gaussians centred at a velocity of 1000 km s^{-1} having dispersions of 20, 40, 60 and 120 km s^{-1} to give four synthetic galaxy spectra for each template. For each of these, an ensemble of 40 noise realizations was created by adding Poisson noise corresponding to SNRs of 10 and 20. The XC method was then applied in exactly the same way as to the observations, using the K0 giant HD 75523 as a template in each case. Fig. 4 shows the XC results, plotting the mean and standard deviation for the output velocities and velocity dispersions in each ensemble. These tests are similar to those performed by Statler (1995), but specifically aim at the low dispersions and SNR typical of galaxy discs.

For the zero-mismatch case (the ensemble created using HD 075523) the random error in both the velocity and velocity dispersion increases with the input velocity dispersion. For the perfect template, the recovery works very well down to small dispersions, even below the spectral pixel size of 26 km s^{-1} (see also Bender 1990). At half the SNR the standard deviations of the ensembles double. These standard deviations agree well with the formal errors of the least-squares fit (Statler 1995).

Mismatch systematically affects the outcome of the XC method. For the mean velocity the systematic error increases with increasing velocity dispersion, reaching values somewhat less than the random error. For galaxy discs, which are observed to have a radially decreasing velocity dispersion, this means that the largest systematic error is expected to occur in the inner parts. The velocity dispersion is more strongly affected. The systematic errors are of the order of 5–10 km s^{-1} and can exceed the random errors. The systematics become severe for the lowest dispersions, those comparable to the instrumental resolution, for which the relative systematic error can reach 50 per cent. This is serious indeed and must be taken into account when interpreting dispersions close to the instrumental resolution. The effect of template mismatch is independent of SNR.

Similar tests using a truncated Gauss–Hermite series revealed the same trends for input dispersions greater than 40 km s^{-1}, but with slightly larger random errors. In those cases the systematic errors

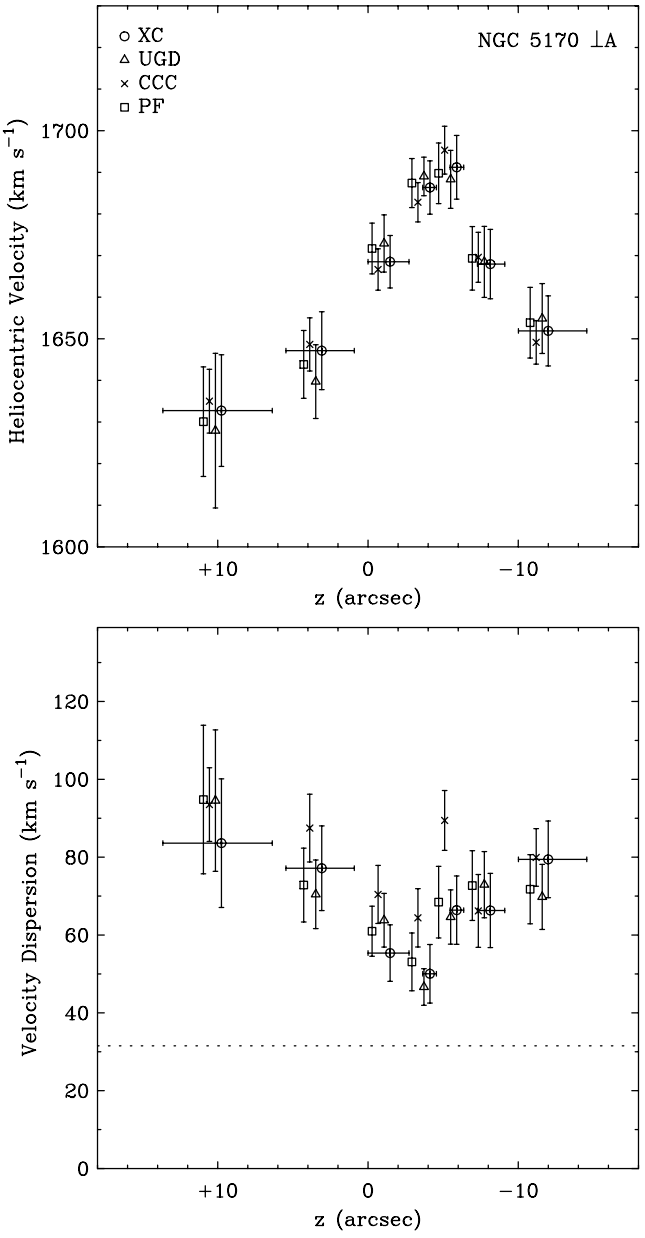

Figure 3. The l.o.s. stellar velocities (top) and velocity dispersions (bottom) of NGC 5170 derived using four different methods (cf. Fig. 5). The horizontal error bars on the XC data denote the amount of averaging along the slit. The data points for the other methods were given a slight offset to the left to facilitate the comparison.

on h_3 and h_4 were $\lesssim 0.05$. However, for input dispersions closer to the instrumental dispersion both the random and systematic errors increase dramatically such that h_3 and h_4 are essentially unmeasurable. At these low dispersions the number of data points in the XCF peak is too small to warrant the use of the truncated Gauss–Hermite series as a fitting model, even at high SNR. The h_4 parameter is often found to be more sensitive to template mismatch, as well as residual large-scale continuum variations (van der Marel & Franx 1993; Statler 1995). The former could not be confirmed using the adopted template stars, probably because they do not cover a large range in spectral type.

4 RESULTS

4.1 The stellar kinematics

The stellar kinematics obtained with the XC method are illustrated in Fig. 5. Table 4 lists the adopted dynamical centre, the slit position and position angle, the SNR per bin, the template star and the type of parametric LOSVD used for each galaxy. For the dynamical centre the position of the apparent optical nucleus in the *I*-band image (table A1 in KKG) was adopted, unless the observed velocity curves of the stars and the emission-line gas (Paper IV) revealed an offset from this position. In that case the offset position was taken (offsets were always within a few arcsec). For NGC 5170 the centre was determined from an *I*-band image obtained at the Jacobus Kapteyn Telescopt (JKT). This image was analysed using the two-dimensional bulge–disc decomposition method of KKG (see Appendix A). For NGC 891 the centre was determined from an *R*-band image, its value being consistent with the centre of the nuclear continuum source (Allen, Baldwin & Sancisi 1978) and the dynamical centre of the CO (Garćia-Burillo et al. 1992). In several galaxies a higher SNR per bin was used in the inner parts to ensure that the bin sizes exceed the seeing element, while further out the lower SNR guarantees that the largest possible radii are reached. At first, a Gaussian LOSVD was used in the XC analysis. Then, for the galaxy spectra with sufficient SNR ($\gtrsim$10) and velocity resolution, the XC analysis was repeated with the truncated Gauss–Hermite series. These results were retained only when the reduced χ^2 of the fits improved. In the following the l.o.s. stellar kinematics will be briefly described for each galaxy.

4.2 Notes on individual galaxies

ESO 142-G24. Both the l.o.s. velocity and l.o.s. velocity dispersion[2] curves are symmetric with respect to the galaxy centre. The velocity dispersion appears to be approximately constant over the measured extent. This may be artificial, given that the dispersions are close to the instrumental resolution.

ESO 157-G18. On the approaching side, the stellar velocity and velocity dispersion are larger. The asymmetry in the velocities is also seen in the H I and the [O III] emission lines (see Paper III).

ESO 201-G22. The velocities are systematically smaller by 10–20 km s^{-1} at the approaching side. Note that the slit was not positioned entirely outside the dust lane.

ESO 240-G11. The stellar kinematics were observed twice, with DBS (position A) and FORS2 (position B). While the stellar velocity dispersions derived from the DBS spectrum are consistent with those derived from the FORS2 spectrum, the stellar velocities are not. For comparison the DBS velocities and velocity dispersions are also shown in the FORS2 panel of Fig. 5 (dots). The DBS observations, taken with a 2-arcsec slit positioned on the major axis, show velocities closely symmetric with respect to the position of the nucleus and the H I systemic velocity. These stellar velocities are in good agreement with the determination of Chung & Bureau (2004). The FORS2 observations, taken with a 0.5-arcsec slit positioned at 2 arcsec from the major axis, reveal velocities that are asymmetric with respect to the galaxy centre, with the velocities at the approaching side being smaller by up to 60 km s^{-1}. A similar velocity difference is observed between the emission-line velocities at both slit positions (see Paper III). Other large-scale peculiarities

[2] Hereafter we simply refer to these properties as velocity and velocity dispersion without the indication 'l.o.s.'.

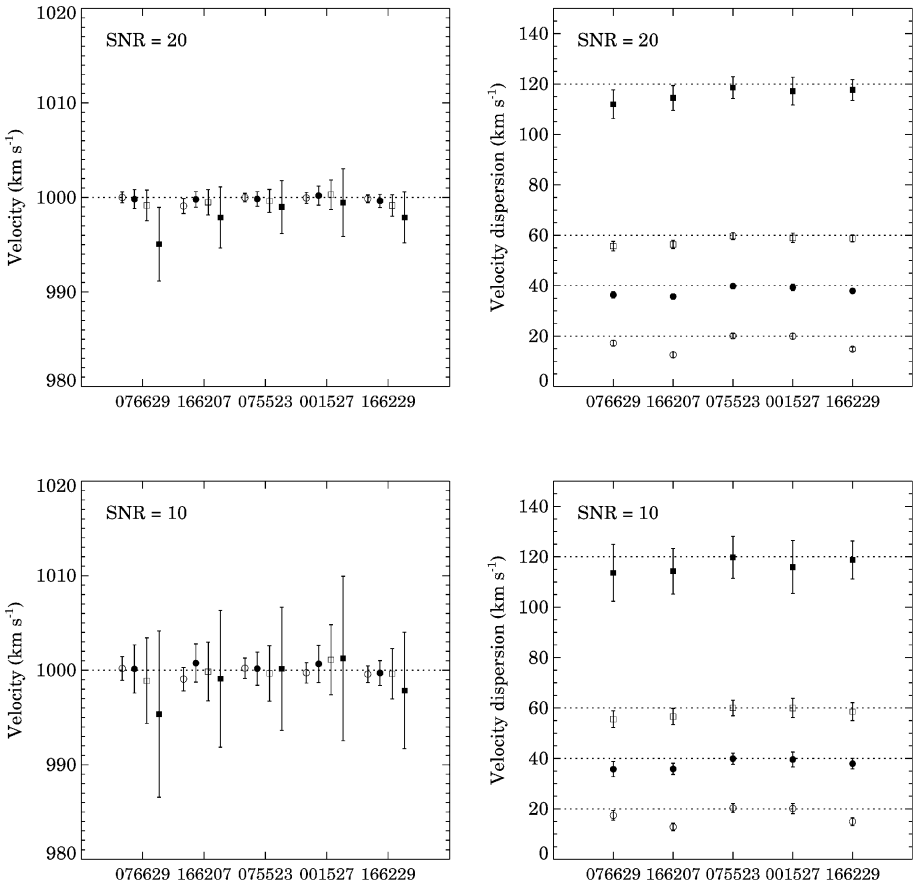

Figure 4. The recovery of the velocity (left) and velocity dispersion (right) for five synthetic galaxy spectra for a SNR of 20 (top) and 10 (bottom) using HD 075523 as a template. Circles denote ensembles with an input velocity dispersion of 20 km s^{-1}, dots denote 40 km s^{-1}, open squares denote 60 km s^{-1} and filled squares denote 120 km s^{-1}.

revealed by the FORS2 data are the larger velocity dispersions on the approaching side and the asymmetric h_4 behaviour with radius (the LOSVDs are more peaked than Gaussian at the receding side). These features and especially the markedly different velocity curves seem to point to a pronounced non-axisymmetric structure within the stellar disc. The change in position angle of the high surface brightness isophotes, from a projected radius of about 20 arcsec to about 40 arcsec (see fig. A1 in KKG), may perhaps be another manifestation of this asymmetry. The 'figure-of-eight' signature seen in the optical emission lines within the inner 10 arcsec suggests that ESO 240-G11 contains a small bar (Bureau & Freeman 1999). This is consistent with the high-velocity tail (i.e. away from the systemic velocity) implied by the h_3 parameter at radii <10 arcsec. Perhaps the small bar is related to the large-scale asymmetry of the disc revealed by the FORS2 data.

ESO 269-G15. There is an offset of 3 arcsec (600 pc) between the optical centre (table A1 in KKG) and the adopted dynamical centre (Table 4 in this paper). The symmetry in the stellar velocity and velocity dispersion curves suggests that this offset is not due to lopsidedness. Perhaps it is caused by dust attenuation affecting the determination of the optical centre.

ESO 288-G25. In essence, the velocity dispersion shows two plateaus, one in the bulge region and the other beyond ∼10 arcsec corresponding to the disc. Since no H I data are available, the systemic velocity was derived by symmetrizing the Hα rotation curve (Paper III).

ESO 416-G25. The prominent boxy bulge of this early-type spiral may dominate the light out to the last measured point. Dust attenuation is unlikely to be important because the slit is positioned far from the dust lane. There is a hint at a double reversal of the h_3 curve similar to that in e.g. ESO 435-G25.

ESO 435-G14. A subtle asymmetry with respect to the galaxy centre is seen in the velocities of the outermost bins, with the velocity flattening off at the receding side and increasing up to the outermost point at the approaching side. The dispersion, on the other hand, is symmetric. The peaks in the slit intensity profile reflect the presence of strong spiral arms seen in the optical image, which are perhaps related to the asymmetry in the velocity curve.

ESO 435-G25. A small plateau is present in the velocity curve at 10 arcsec. The velocity dispersion shows a rather steep drop at small radii followed by a much more gradual decline starting at ∼20 arcsec. The h_3 curve shows a conspicuous signature. This signature is also seen in at least three other galaxies and will be discussed in Section 5. Note that the h_3 goes through the origin, suggesting that template mismatch is not a problem.

ESO 437-G62. The poor quality of the H I data (Paper III) did not allow a determination of the systemic velocity. Instead, the dynamical centre and systemic velocity were determined by symmetrizing the stellar velocity curve. The observed kinematics may be influenced by dust attenuation since, unfortunately, the slit was positioned 'on' the dust lane during the service observing. The h_3 and h_4 curves show remarkably strong deviations from Gaussianity

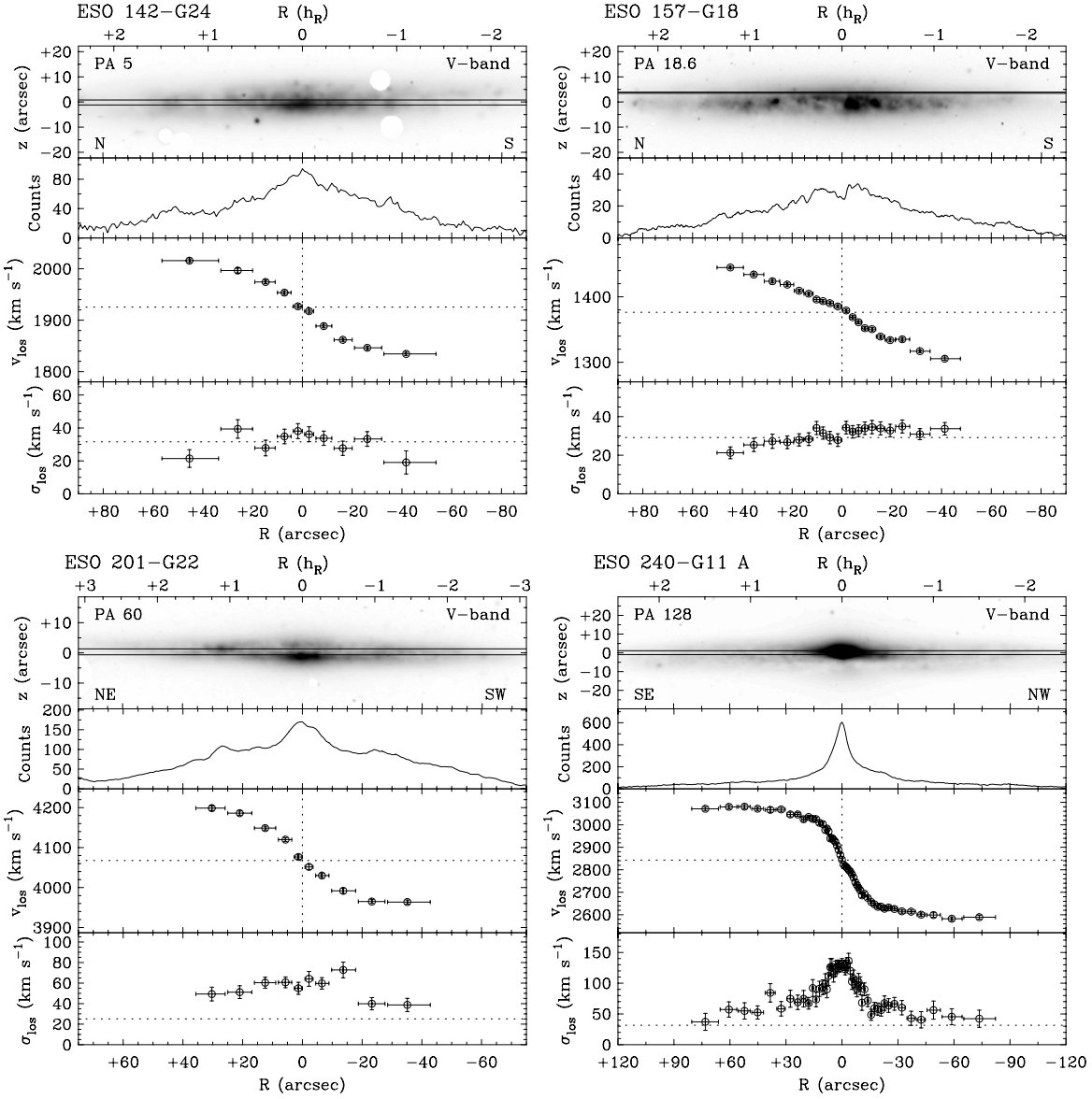

Figure 5. Line-of-sight stellar kinematics for the full sample. For each galaxy, the upper panel shows an optical image, rotated such that the major axis is horizontal and the receding side is to the left. The top axis is units of I-band scalelengths (table 1 in KKG). Two solid lines represent the slit jaws. The image passband and the slit position angle are indicated. The second panel shows the average number of counts in the spectra per spectral pixel. The third panel shows the mean l.o.s. stellar velocity (heliocentric). Data are plotted at the intensity-weighted mean position of each bin, with the horizontal error bars indicating the bin size. The horizontal and vertical dotted lines indicate the H I systemic velocity (from Paper II) and the dynamical centre (Table 4), respectively. The fourth panel displays the l.o.s. stellar velocity dispersion. The horizontal dotted line indicates the velocity shift per pixel. In cases where the truncated Gauss–Hermite series was used, the fifth and sixth panels show the h_3 and h_4 parameters.

(Section 5). The stellar kinematics are highly symmetric with respect to the centre, in contrast with the optical emission-line kinematics (Bureau & Freeman 1999).

ESO 446-G18. Unfortunately, the slit was positioned 'on' the dust lane during the service observing. The mean velocity curve is still rising rather steeply in the inner bulge-dominated region, while the decrease in velocity dispersion is steep compared with other galaxies in the sample. The h_3 and h_4 show no strong radial variation.

ESO 487-G02. For the systemic velocity a value of 1753.7 km s^{-1} was adopted (LEDA). Owing to a low SNR, all the emission along the slit had to be averaged in the analysis, including the prominent dust lane. The better quality data of the vertical slits for NGC 891 and 5170 indicate that this averaging tends to decrease the observed velocity and velocity dispersion. This effect will be estimated when modelling the observed kinematics.

ESO 509-G19. Both the velocity and dispersion are fairly symmetric, although the data cover a rather limited radial range. This huge spiral is of importance because it greatly extends the range in maximal rotational velocity and disc size covered by the sample.

ESO 564-G27. Unfortunately, the spatial sampling is rather poor because of the low SNR of the spectra and the presence of two bright foreground stars on the major axis. The velocity dispersions approach the instrumental resolution beyond ~ 20 arcsec.

NGC 891. The slit positioned perpendicular to the major axis indicates that the kinematics are rather symmetric with respect to the

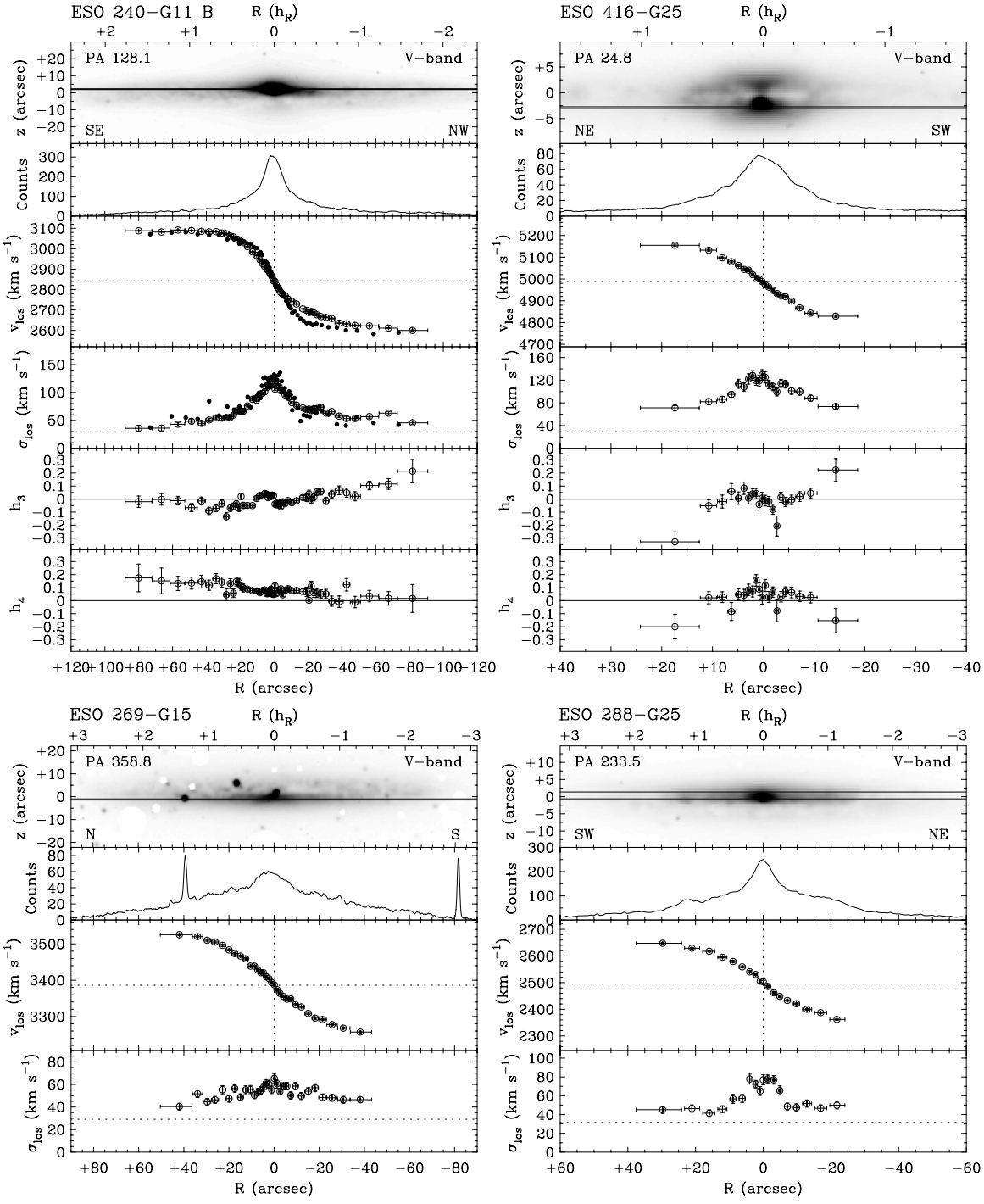

Figure 5 – *continued*

galactic plane ($z = 0$). Both the velocities and velocity dispersions show a clear drop below $z \simeq h_z$ with minima at $z = 0$. This behaviour is probably caused by dust attenuation. A high optical depth near the plane would largely hide the region at the line of nodes (the intersection of the galaxy plane and the plane of the sky). Only the outskirts of the stellar disc nearer to the observer, which are expected to have small projected velocities and velocity dispersions, still contribute to the LOSVD. Above the strong dust lane ($z \geqslant h_z$), the stellar velocities and dispersions remain constant with z up to $\simeq 2.5\, h_z$. The slit positioned parallel to the major axis reveals a steady radial decrease of the velocity dispersion. In addition, several small-scale irregularities in the stellar velocity and dispersion are apparent, for instance at $R = -110$ arcsec. These irregularities can be traced to distinct dust patches in the optical image. The h_3 parameter reveals a high-velocity tail in the LOSVD for radii up to 50 arcsec. The h_4 parameter seems to indicate that the LOSVD is more peaked than Gaussian in this region.

NGC 5170. The stellar kinematics at slit position A show a maximum in the velocity and, at the same position, a minimum in the dispersion. The fact that this position is offset from the major axis is

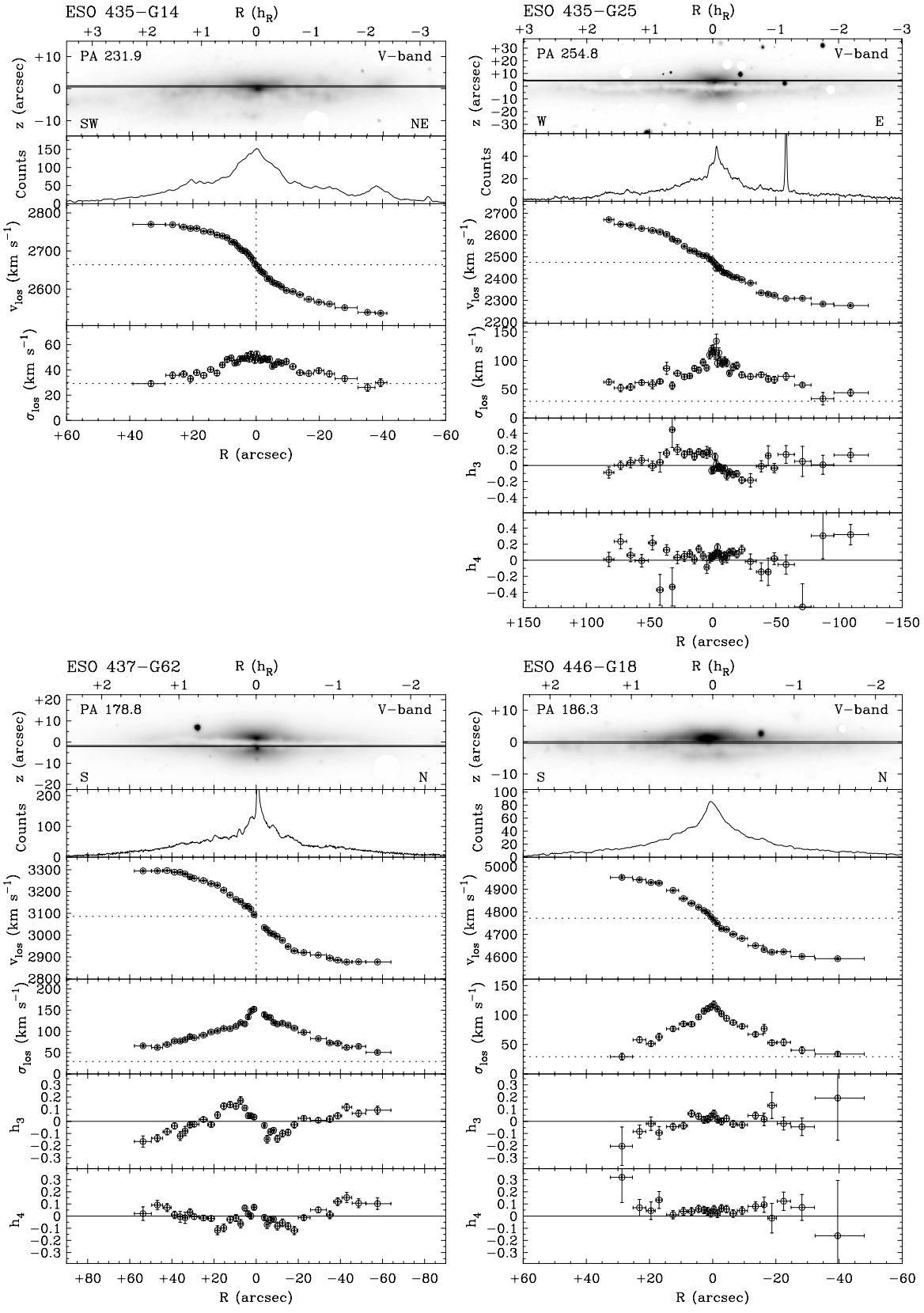

Figure 5 – *continued*

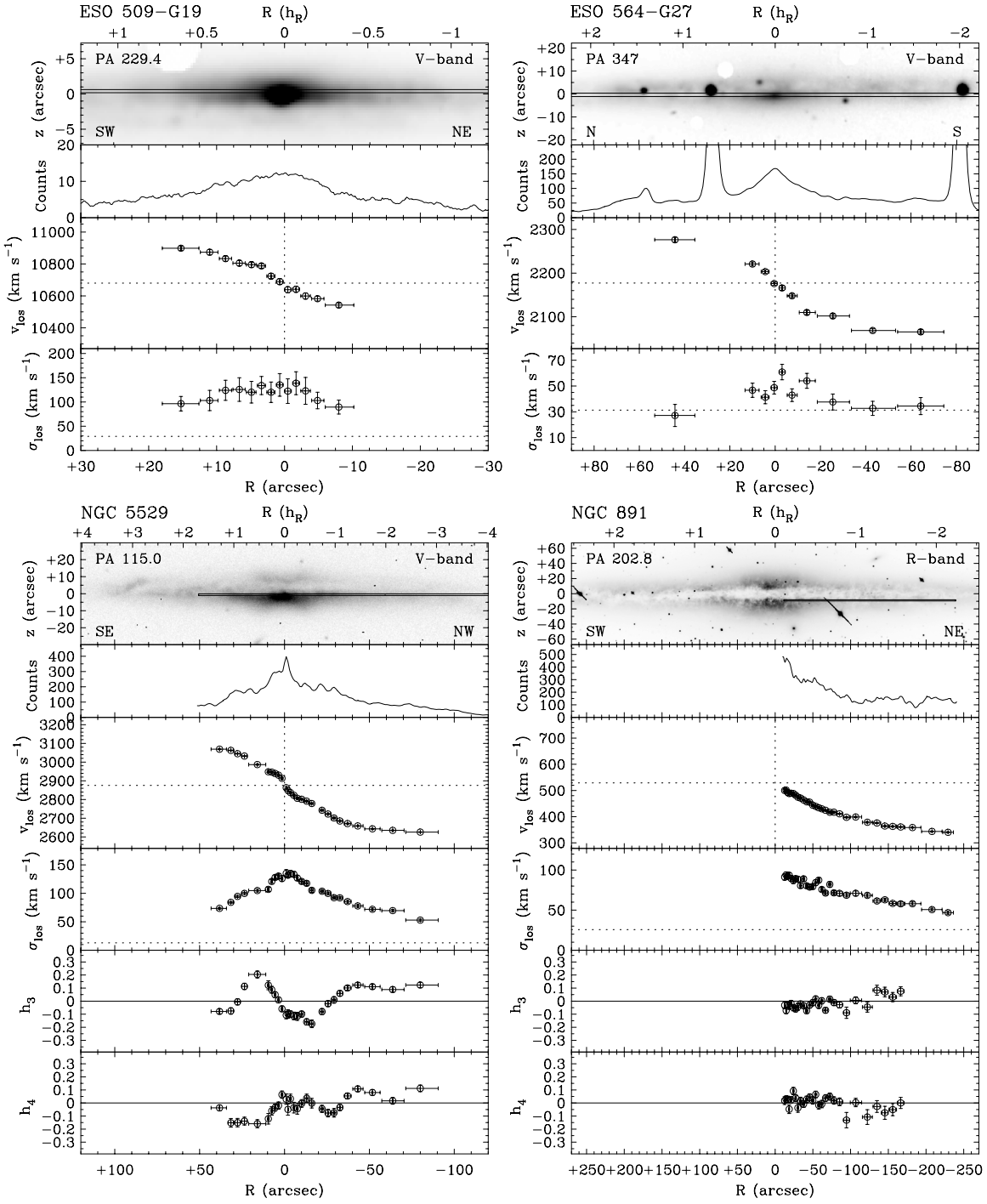

Figure 5 – *continued*

probably related to the slight tilt of NGC 5170 away from edge-on. At position B the kinematics are sparsely sampled and shows no clear trend with z.

NGC 5529. The velocity curve is asymmetric. On the approaching side, it reaches a distinct plateau at projected radii around 10 arcsec, then rises sharply and slowly flattens out to the last measured point at 3 scalelengths. The central velocity dispersion is the largest in the sample, and declines slowly with projected radius. The h_3 and h_4 parameters reveal very strong asymmetries in the velocity profiles and show several sign reversals with projected radius.

5 DISCUSSION

5.1 General properties

As an overview, Fig. 6 shows simultaneously the velocity and velocity dispersion curves for all the galaxies for which a spectrum was taken parallel to the major axis. To facilitate a meaningful comparison the data are plotted in units of I-band disc scalelengths. In most cases the data extend well into the disc-dominated region, the last-measured point corresponding to a projected radius between

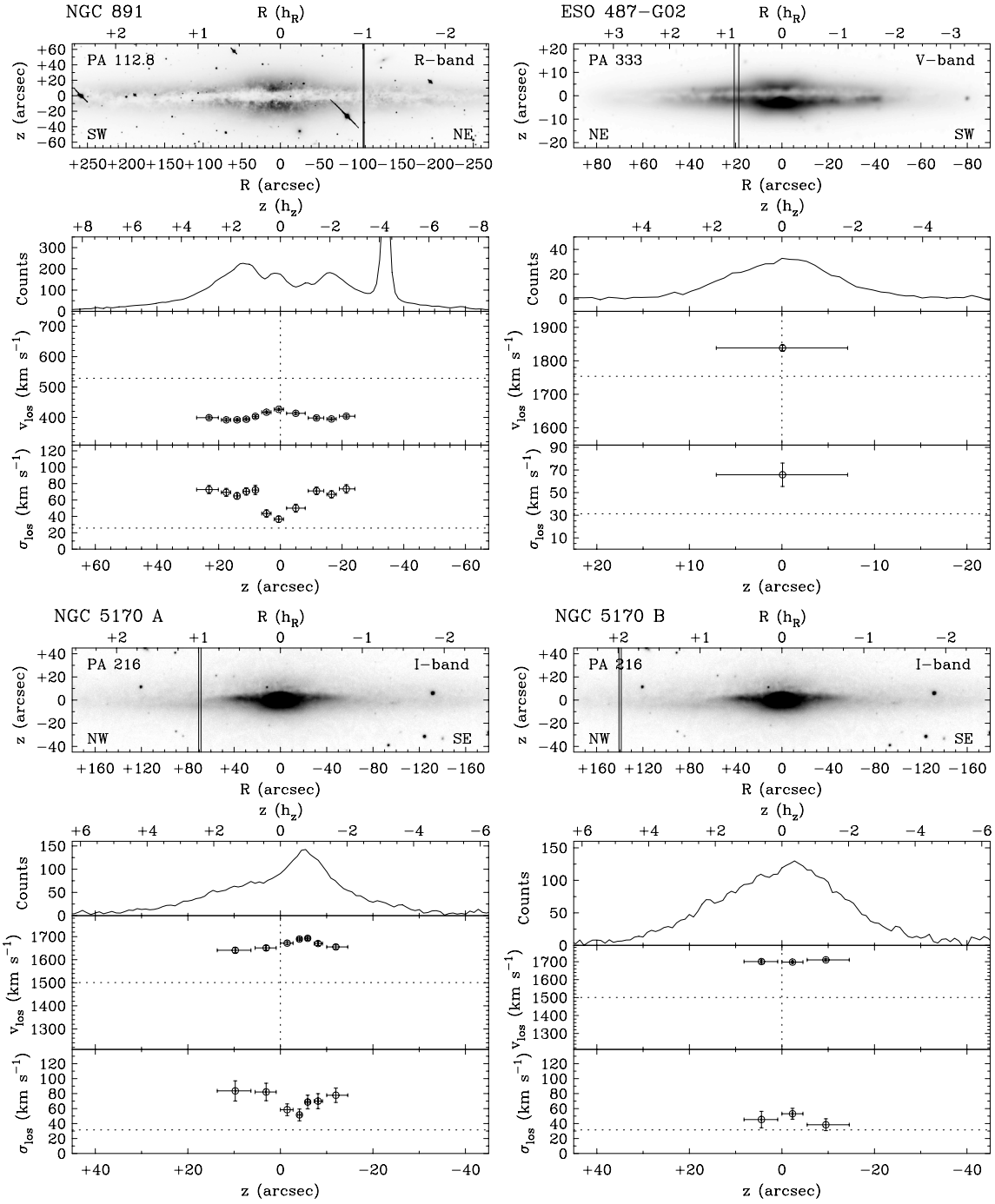

Figure 5 – *continued*

1 and 2.5 disc scalelengths. The exceptions are ESO 416-G25 and 509-G19, for which the data are mainly confined to the bulge region (data up to 0.5 scalelengths). Viewing the entire sample, there is no strong systematic difference between the l.o.s. stellar kinematics on the approaching and the receding sides. However, there are substantial differences in a few individual cases, most notably ESO 157-G18 and 240-G11 (Section 4.2). These kinematic asymmetries are most clearly seen in the stellar velocity. These differences may arise from strong non-axisymmetric structures in the disc, e.g. in the form of a bar, lopsidedness or spiral arms. Note that an asymmetry in the l.o.s. velocity is expected in case of template mismatch, because a mismatch-induced error is expected to have the same sign independently of position. The fact that any asymmetries observed in the stellar velocity curve are also seen in the H II kinematics (Paper III) provides direct evidence that the effect of template mismatch is small.

Although the parametrization of the stellar kinematics does not present a direct view of the intrinsic stellar disc rotation and velocity dispersion, the l.o.s. velocity and velocity dispersion curves already show several important features. First, none of the galaxies in Fig. 6 exhibits a velocity curve of solid-body (linear) form. This simple observation implies that the stellar discs are all differentially

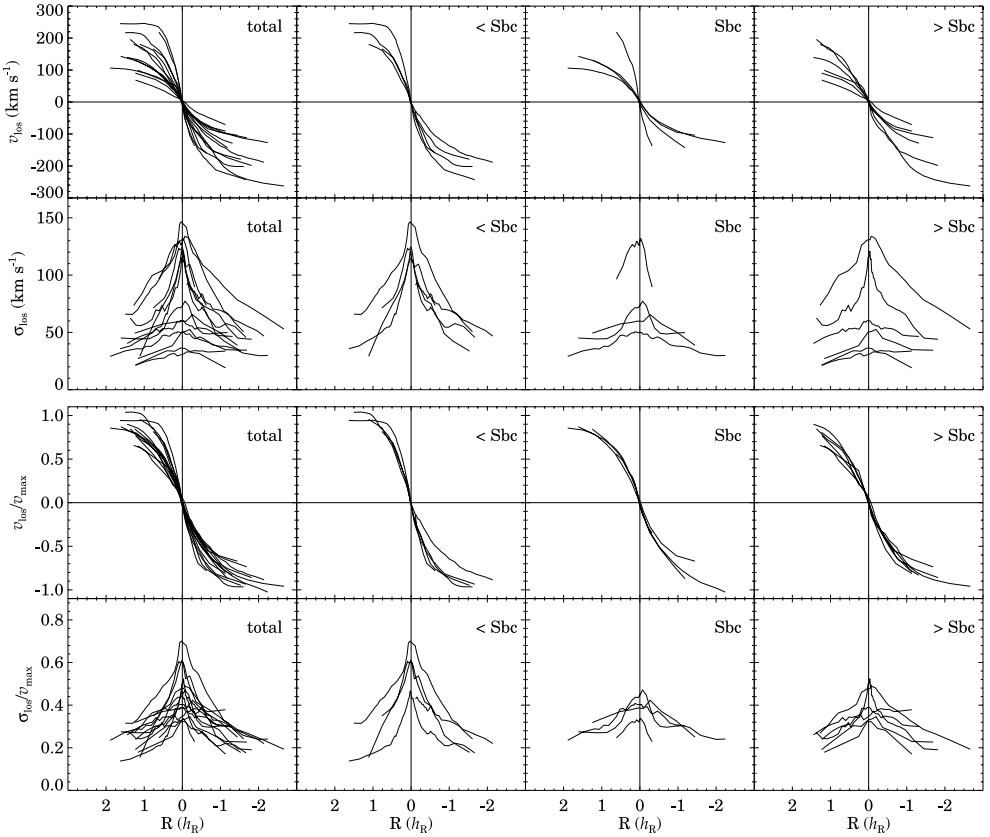

Figure 6. The l.o.s. velocities and velocity dispersions for the 15 galaxies for which the slit was positioned parallel to the galaxy major axis (top rows). The same data are also shown after dividing by the maximum rotational velocity (LEDA) (bottom rows). In each row, the first panel shows the total sample, while in the other panels the galaxies are binned according to morphological type (LEDA). The abscissa is in units of scalelengths.

rotating. More importantly, a high optical depth would lead to a solid-body velocity curve (Bosma et al. 1992). Hence the fact that no solid-body curves are observed also shows that dust extinction is not strongly affecting the observed LOSVDs. Note, however, that strong dust extinction can have a large effect of the LOSVD, as in NGC 891 at z-heights smaller than one vertical scaleheight ($z < h_z$, Fig. 5). This appears to justify our strategy of positioning the slit outside the main dust lane to avoid the bulk of the dust (see also Baes et al. 2003). A quantification of the extent to which dust attenuation influences the observed stellar kinematics is deferred to Paper III, where the optical emission-line kinematics will be studied and compared with the kinematics of the optically thin H I line. Besides the fact that none of the curves is of solid-body form, there is a large variety in the amplitudes and the shapes of the curves.

The l.o.s. velocity dispersions cover a substantial range in amplitude, with central dispersions of 20–150 km s^{-1}. In most galaxies the l.o.s. stellar velocity dispersion clearly decreases with projected radius, also outside the central bulge region ($R \gtrsim 0.5\ h_R$). Nice examples are ESO 435-G14, ESO 437-G62, NGC 891 and NGC 5529. For some galaxies the data outside the bulge region instead suggest a l.o.s. dispersion constant with projected radius (e.g. ESO 142-G24 and 288-G25). However, in these cases the velocity dispersion is close to the instrumental resolution, where the systematic errors due to template mismatch may be substantial (Section 3.5). It appears that the data are consistent with the radially declining intrinsic stellar disc velocity dispersions measured in less-inclined spirals (Bottema 1993; Gerssen et al. 1997, 2000). However, part of the decline may also be due to the l.o.s. projection: modelling of the l.o.s. stellar kinematics is required to firmly address this question.

5.2 A σ–v_{max} relation for discs?

There is no strict trend of the l.o.s. velocity dispersion with morphological type, although later type spirals generally have smaller σ_{los}/v_{max} (Fig. 6). This trend can be ascribed to the decreasing bulge contribution: (1) bulges have larger stellar velocity dispersions than discs and, when dominant, will cause a higher l.o.s. velocity dispersion in the central parts; (2) early-type spirals generally have steeper circular velocity curves causing a larger l.o.s. velocity gradient in the inner parts. In contrast, at 1 disc scalelength, where the disc dominates, the range in l.o.s. velocity dispersions is rather narrow: $\sigma_{los}(h_R) = (0.2\text{–}0.4)v_{max}$. Fig. 7(a) visualizes this observation in a different way, showing the l.o.s. velocity dispersion at 1 disc scalelength versus the maximum rotational velocity. This relation is not due to dust extinction. First, as discussed above, the effect of dust extinction is not large because the stellar rotation curves are far from solid-body. Secondly, because dust extinction reduces the l.o.s. stellar velocity dispersion (see notes for NGC 891 in Section 4.2 and the corresponding panel in Fig. 5), Fig. 7(a) would imply that extinction progressively increases towards spirals with smaller v_{max}. This is contrary to what is inferred (Giovanelli et al. 1995; Tully et al. 1998).

Observations of the stellar kinematics in 11 HSB spirals of various inclination show a relation very similar to that of Fig. 7(a), but for

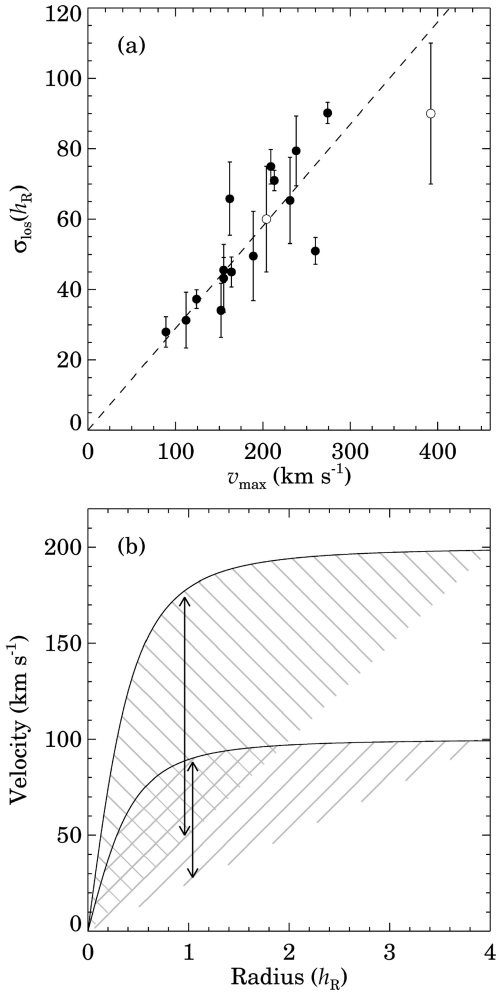

Figure 7. (a) The line-of-sight velocity dispersion at one I-band scalelength versus maximum rotational velocity (LEDA). The values for ESO 416-G25 and 509-G19 are based on a visual extrapolation (circles). The dashed line indicates the relation between the *intrinsic* radial velocity dispersion at h_R and the maximal rotational velocity in HSB spirals (Bottema 1993). (b) Sketch illustrating the increase of the width of the stellar LOSVD for a larger maximal rotational velocity in dynamically cold edge-on discs with a truncation at $4h_R$. Solid lines show the intrinsic stellar rotation curves. Hatched regions indicate the range covered by the l.o.s. stellar velocities. The arrows indicate the velocity width.

the *intrinsic* radial velocity dispersion (Bottema 1993; KKG):

$$\sigma_R(h_R) = (0.29 \pm 0.10) v_{max}. \quad (3)$$

Does the correlation seen in Fig. 7(a) reflect this σ_R–v_{max} relation? In Paper IV, an ensemble of exponential stellar disc models will be studied with respect to the effect of the l.o.s. projection on the observable kinematics. For a range of rotation curve shapes these models show that the l.o.s. velocity dispersion at 1 disc scalelength is comparable to the intrinsic radial velocity dispersion $\sigma_R(h_R)$. Hence, if the σ_R–v_{max} relation (equation 3) holds for all stellar discs, it will probably also be visible in our data. There is an important caveat, however. For stellar discs that are dynamically colder, $\sigma_R(h_R)/v_{max} \lesssim 0.2$, the dispersion in the l.o.s. velocities of the stars is mainly due to the gradient in the l.o.s. rotational velocity. In that case a galaxy with a larger maximum rotational velocity will have a larger l.o.s. velocity dispersion (that is, a broader observed line profile) simply because of the projection (Fig. 7b). This causes a correlation between σ_{los} and v_{max} with a slope similar to that observed in Fig. 7(a). We conclude that, although it is possible that the correlation seen in Fig. 7 represents the σ_R–v_{max} relation observed by Bottema (1993), proper modelling of the stellar kinematics is required to firmly address this question. We will return to this in Papers IV and V.

5.3 Non-Gaussian LOSVDs

An examination of the h_3 and h_4 curves of the seven galaxies for which the Gauss–Hermite parametrization could be used (Table 4) reveals that four clearly show a common signature in the h_3 parameter. These galaxies, ESO 240-G11, ESO 435-G25, ESO 437-G62 and NGC 5529, show a low-velocity tail at large radii and a high-velocity tail at small radii. Three of these also show a common signature in the h_4 parameter (ESO 435-G25, ESO 437-G62 and NGC 5529): a LOSVD that is more peaked than Gaussian at large radii, less peaked at intermediate radii and again more peaked in the very central region. Moreover, in ESO 435-G25, ESO 437-G62 and especially NGC 5529 the mean stellar velocity shows a small plateau in the central region. Two other galaxies, ESO 416-G25 and NGC 891, appear to show similar weaker features, although the radial range covered by the data is less in these cases. All of these spirals have a boxy- or peanut-shaped bulge.

Since the high-velocity tails occur at small projected radii, it is tempting to identify the asymmetric velocity distributions with a bar. A barred potential induces a lack of possible orbits near corotation, which in the edge-on view results in LOSVDs with a 'figure-of-eight' or 'X' appearance with projected radius (Kuijken & Merrifield 1995; Bureau & Athanassoula 1999; Athanassoula & Bureau 1999). This feature has been detected in the velocity distributions of ionized gas and stars in several edge-on spirals with a boxy- or peanut-shaped bulge (Kuijken & Merrifield 1995; Bureau & Freeman 1999), suggesting that these bulges are associated with bars. The signatures seen in the l.o.s. velocity, h_3 and h_4 would then need to represent this 'figure-of-eight'. Indeed, ESO 240-G11 (see also Bureau & Freeman 1999) and NGC 5529 clearly show this signature in the optical emission lines (see Paper III), suggesting that these spirals are barred.

However, a similar conspicuous signature in the h_3 and h_4 curves is seen in the projected kinematics of a pure exponential disc, as we will see in Paper IV. Consider the h_3 parameter. At large projected radii the high-density material at the line of nodes, for which the l.o.s. velocity equals the circular velocity, dominates the LOSVD while the remaining low-density material forms a low-velocity tail. However, contrary to common belief (e.g. Kuijken & Merrifield 1995), this behaviour does not continue down to $R = 0$. Instead, an exponential disc causes a high-velocity tail at small projected radii due to the increasing velocity crowding of low-density material. Unfortunately, the spectra of the bulgeless spirals in the current sample do not have the SNR and/or spectral sampling to show this observationally. None the less, the exponential disc model studied in Paper IV suggests that the occurrence of the h_3 and h_4 signatures alone cannot be used to infer the presence of a bar. The plateau seen in the mean velocity curve at small radii is not present in the projection of an exponential disc. Perhaps this signature can be used instead to establish unequivocally the bar connection. Finally, note that all the h_3 curves nicely reverse sign at the dynamical centre. This indicates that the effect of template mismatch is small.

6 SUMMARY

In this first paper of a series aiming to study the stellar dynamics of galaxy discs, we have presented deep optical long-slit spectra of 17 edge-on spiral galaxies of intermediate to late morphological type. In the next papers we will present H I synthesis observations of these galaxies (Paper II), analyse these data together with our Hα data to determine the circular velocity curves (Paper III), and correct the stellar data described here for the line-of-sight effects (Paper IV). Finally in Paper V we will discuss our findings in terms of the issues mentioned in the intriduction.

Most of the spectra have been taken parallel to and away from the galaxy major axis to study the radial variation of the stellar kinematics. For three galaxies the slit was positioned perpendicular to the major axis to investigate the variation of the stellar kinematics with height above the galaxy plane. The line-of-sight (l.o.s.) stellar kinematics have been extracted from the stellar absorption lines in the 4800–5800 Å region using the cross-correlation technique. For 15 galaxies the derived l.o.s. stellar kinematics reach well into the disc region and are well suited for a study of the intrinsic stellar disc kinematics.

None of the l.o.s. stellar velocity curves has a solid-body shape, showing that the stellar discs are differentially rotating and, more importantly, that the effect of dust attenuation is not large. A more quantitative analysis of the effect of dust extinction on our observations is postponed to Papers III and IV. The l.o.s. stellar disc velocity dispersions decrease with radius, in qualitative agreement with the trends observed in less-inclined spirals. We find that the l.o.s. stellar disc velocity dispersion correlates strongly with maximum rotational velocity. A deprojection of the l.o.s. stellar kinematics is necessary to establish whether this correlation reflects the σ–$v_{\rm max}$ relation observed in less-inclined spirals (Bottema 1993) or is due to the projection.

At least four of the seven spirals for which the Gauss–Hermite parametrization could be used have asymmetric LOSVDs, with a localized plateau in the l.o.s. stellar velocity curve and a common signature in the h_3 and h_4 parameters with projected radius. All of these have either a boxy- or peanut-shaped bulge. For ESO 240-G11 and NGC 5529 a 'figure-of-eight' feature is present in the optical emission lines, showing that their discs are probably barred. This would suggest that in general the asymmetries seen in the Gauss–Hermite parameters are linked to the presence of a bar. However, a pure exponential disc shows asymmetries in the h_3 and h_4 parameters reminiscent of those observed.

ACKNOWLEDGMENTS

MK thanks Roelof Bottema and Koen Kuijken for discussions and acknowledges the hospitality at Mount Stromlo Observatory on a work visit. The Leids Kerkhoven–Bosscha Fonds is acknowledged for providing financial support. PCvdK thanks the Mount Stromlo and Siding Spring Observatories for hospitality during a number of visits and the Area Board for Exact Sciences of the Netherlands Organization for Scientific Research (NWO) for financial support. Rob Swaters and Edo Noordermeer are thanked for sharing the optical images of NGC 891 and 5170. Tom Statler is acknowledged for making his cross-correlation software available. This paper is based on observations at the Siding Spring Observatory of the Australian National University run by the RSAA, and on observations made with ESO Telescopes at the La Silla and Paranal Observatories under programme ID 66.B-0267A. The William Herschel Telescope and the Jacobus Kapteyn Telescope are operated on behalf of PPARC, NWO and IAC at the Roque de Los Muchachos Observatory, La Palma, Spain. The data analysis was performed using IRAF, distributed by NOAO, MIDAS, distributed by ESO, and IDL. We have made use of the LEDA data base, recently incorporated in HyperLeda.

REFERENCES

Allen R. J., Baldwin J. E., Sancisi R., 1978, A&A, 62, 397
Athanassoula E., Bureau M., 1999, ApJ, 552, 699
Baes M. et al., 2003, MNRAS, 343, 1081
Bender R., 1990, A&A, 229, 441
Bosma A., Byun Y., Freeman K. C., Athanassoula E., 1992, ApJ, 400, 21
Bottema R., 1988, A&A, 197, 105
Bottema R., 1993, A&A, 275, 16
Bottema R., 1999, A&A, 348, 77
Bottema R., van der Kruit P. C., Freeman K. C., 1987, A&A, 178, 77
Bottema R., van der Kruit P. C., Valentijn E. A., 1991, A&A, 247, 357
Brault J. W., White O. R., 1971, A&A, 13, 169
Bureau M., Athanassoula E., 1999, ApJ, 552, 686
Bureau M., Freeman K. C., 1999, AJ, 118, 126
Chung A., Bureau M., 2004, AJ, in press
Da Costa G. S., Jerjen H., 2002, eds, ASP Conf. Ser. Vol. 273, The dynamics, structure and history of galaxies. Astron. Soc. Pac., San Francisco
de Bruyne V., Vauterin P., de Rijcke S., Dejonghe H., 2003, MNRAS, 339, 215
de Grijs R., 1997, PhD thesis, University of Groningen (http://www.ub.rug.nl/eldoc/dis/science/r.de.grijs)
de Grijs R., 1998, MNRAS, 299, 595
Franx M., Illingworth G. D., 1988, ApJ, 327, 55
García-Burillo S., Guélin M., Cernicharo J., Dahlem M., 1992, A&A, 266, 21
Gerssen J., Kuijken K., Merrifield M. R., 1997, MNRAS, 288, 618
Gerssen J., Kuijken K., Merrifield M. R., 2000, MNRAS, 317, 545
Giovanelli R., Haynes M. P., Salzer J. J., Wegner G., Da Costa L. N., Freudling W., 1995, AJ, 110, 1059
Kregel M., 2003, PhD thesis, University of Groningen (http://www.ub.rug.nl/eldoc/dis/science/m.kregel)
Kregel M., van der Kruit P. C., 2004, MNRAS, submitted
Kregel M., van der Kruit P. C., de Grijs R., 2002, MNRAS, 334, 646 (KKG)
Kregel M., van der Kruit P. C., de Blok W. J. G., 2004, MNRAS, submitted
Kuijken K., Merrifield M. R., 1993, MNRAS, 264, 712
Kuijken K., Merrifield M. R., 1995, ApJ, 443, L13
Martin C. L., Kennicutt R. C., 2001, ApJ, 555, 301
Mathewson D. S., Ford V. L., 1996, ApJS, 107, 97
Nelder J. A., Mead R., 1965, Comput. J., 7, 308
Pignatelli E. et al., 2001, MNRAS, 323, 188
Rix H.-W., White S. D. M., 1992, MNRAS, 254, 389
Simkin S. M., 1974, A&A, 31, 129
Statler T. S., 1995, AJ, 109, 1371
Tonry J., Davis M., 1979, AJ, 84, 1511
Tully R. B., Pierce M. J., Huang J. S., Saunders W., Verheijen M. A. W., Witchalls P. L., 1998, AJ, 115, 2264
van der Kruit P. C., Freeman K. C., 1986, ApJ, 303, 556
van der Kruit P. C., Searle L., 1981a, A&A, 95, 105
van der Kruit P. C., Searle L., 1981b, A&A, 95, 116
van der Kruit P. C., Searle L., 1982, A&A, 110, 61
van der Marel R. P., 1994, MNRAS, 270, 271
van der Marel R. P., Franx M., 1993, ApJ, 407, 525
Wang B., Silk J., 1994, ApJ, 427, 759
Xilouris E. M., Byun Y. I., Kylafis N. D., Paleologou E. V., Papamastorakis J., 1999, A&A, 344, 868
Zasov A. V., Bizyaev D. V., Makarov D. I., Tyurina N. V., 2002, Astron. Lett., 28, 527

APPENDIX A: 2D BULGE–DISC DECOMPOSITION OF NGC 5170

No good-quality surface photometry is available in the literature for NGC 5170. For our analysis in further papers we need similar

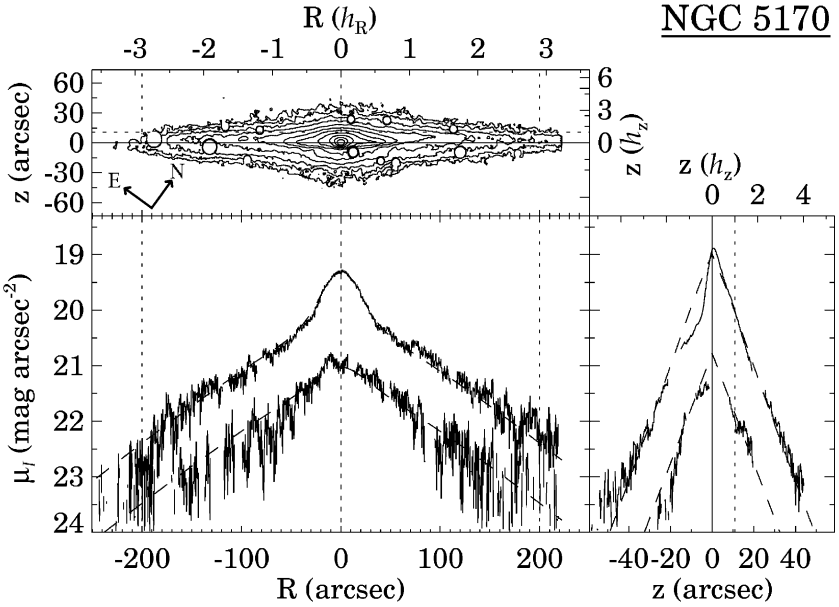

Figure A1. Results of the 2D bulge–disc decomposition applied to the JKT *I*-band image of NGC 5170. Top: surface brightness distribution – contour levels are in steps of 0.5 mag, starting with 22.2 mag arcsec^{-2} at the lowest contour. Lower left: profiles extracted parallel to the major axis at 1 and 2 scaleheights after averaging over 1/3 scaleheights. Lower right: profiles extracted parallel to the minor axis at 0.5 and 2.5 scalelengths after averaging over 1/2 scalelengths. In both lower panels the dashed line shows the best-fitting model. The dotted lines indicate the adopted fitting boundaries.

photometric data to those for other galaxies in the sample. Therefore we analysed an image of NGC 5170 following the procedures of KKG. Observations of NGC 5170 were carried out on 2000 May 31 using the direct-imaging mode of the JKT on La Palma. The JKT was operated with a 2048^2 SITe CCD (0.330 arcsec pixel^{-1}, effective field of view ∼8 arcmin). The galaxy was observed for 2 × 900 s using the Harris *I*-band filter. Data reduction was carried out following standard IRAF procedures. After combining the images, the sky level was determined by fitting a low-order 2D polynomial to the background (making sure the regions containing objects were excluded) and subtracting. The image was calibrated using $m_I^0 = 9.66$ mag (Mathewson & Ford 1996, corrected for Galactic extinction).

Further preparations of the galaxy image followed the same procedures as in KKG, including rotating the image to align the major axis with the image rows (using a major axis position angle of 126°) and masking. For the galaxy centre the position of the nucleus was adopted (Table 4). Then, a bulge–disc decomposition was performed according to the 2D fitting method (KKG), using initial estimates obtained from 1D fits to the major and minor axis profiles. Since the south-western side is clearly affected by dust attenuation, only the north-eastern (far) side was included in the 2D fit. Data below 1 scaleheight were masked out using an iterative approach (see KKG for details). The best fit was found for an exponential bulge, although the corresponding reduced χ^2 is only marginally lower than that obtained with an $r^{1/4}$ bulge. The data and best-fitting model are illustrated in Fig. A1 in the same format as was used in KKG. The derived parameters are $\mu_0^{\text{edge-on}} = 18.7 \pm 0.3$ mag arcsec^{-2}, $h_R = 70 \pm 15$ arcsec, $h_z = 9 \pm 2$ arcsec, $\mu_e = 18.5 \pm 0.3$ mag arcsec^{-2}, $r_e = 15 \pm 4$ arcsec and $q = 0.53 \pm 0.06$ (see KKG for the definitions of these parameters).

This paper has been typeset from a TEX/LATEX file prepared by the author.